Acta Oceanol. Sin., 2022, Vol. 41, No. 10, P. 41–53
https://doi.org/10.1007/s13131-022-2012-6
http://www.aosocean.com
E-mail: ocean2@hyxb.org.cn

Modified parameterization for near-inertial waves

Weiqi Hong[1], Lei Zhou[1, 2*], Xiaohui Xie[1, 2, 3], Han Zhang[2, 3, 4], Changrong Liang[5]

[1] School of Oceanography, Shanghai Jiao Tong University, Shanghai 200030, China

[2] Southern Marine Science and Engineering Guangdong Laboratory (Zhuhai), Zhuhai 519082, China

[3] State Key Laboratory of Satellite Ocean Environment Dynamics, Second Institute of Oceanography, Ministry of Natural Resources, Hangzhou 310012, China

[4] Fujian Provincial Key Laboratory for Coastal Ecology and Environmental Studies, Xiamen University, Xiamen 361102, China

[5] State Key Laboratory of Tropical Oceanography, South China Sea Institute of Oceanology, Chinese Academy of Sciences, Guangzhou 510301, China

Received 24 January 2022; accepted 27 January 2022

© Chinese Society for Oceanography and Springer-Verlag GmbH Germany, part of Springer Nature 2022

Abstract

The near-inertial waves (NIWs) are important for energy cascade in the ocean. They are usually significantly reinforced by strong winds, such as typhoon. Due to relatively coarse resolutions in contemporary climate models, NIWs and associated ocean mixing need to be parameterized. In this study, a parameterization for NIWs proposed by Jochum in 2013 (J13 scheme), which has been widely used, is compared with the observations in the South China Sea, and the observations are treated as model outputs. Under normal conditions, the J13 scheme performs well. However, there are noticeable discrepancies between the J13 scheme and observations during typhoon. During Typhoon Kalmaegi in 2014, the inferred value of the boundary layer is deeper in the J13 scheme due to the weak near-inertial velocity shear in the vertical. After typhoon, the spreading of NIWs beneath the upper boundary layer is much faster than the theoretical prediction of inertial gravity waves, and this fast process is not rendered well by the J13 scheme. In addition, below the boundary layer, NIWs and associated diapycnal mixing last longer than the direct impacts of typhoon on the sea surface. Since the energy dissipation and diapycnal mixing below the boundary layer are bounded to the surface winds in the J13 scheme, the prolonged influences of typhoon via NIWs in the ocean interior are missing in this scheme. Based on current examination, modifications to the J13 scheme are proposed, and the modified version can reduce the discrepancies in the temporal and vertical structures of diapycnal mixing.

Key words: near-inertial waves, parameterization, ocean mixing, upper ocean boundary layer, typhoon

Citation: Hong Weiqi, Zhou Lei, Xie Xiaohui, Zhang Han, Liang Changrong. 2022. Modified parameterization for near-inertial waves. Acta Oceanologica Sinica, 41(10): 41–53, doi: 10.1007/s13131-022-2012-6

1 Introduction

Near-inertial waves (NIWs) are the internal gravity waves with a frequency around the inertial frequency ($f = 2\Omega\sin\phi$; where ϕ is the latitude, Ω=7.29×10^{-5} rad/s), which are ubiquitous in the ocean interior (Alford et al., 2016; Webster, 1968). NIW is a major funnel for wind energy that goes into the ocean and about 2/3 of near-inertial energy is generated due to surface wind forcing (Fu, 1981). It is estimated that the wind energy of 0.3–0.7 TW (1 TW=10^{12} W) enters the upper ocean via NIWs every year (Alford, 2020; Watanabe and Hibiya, 2002) which is approximately 1/6 of the total energy flux (~3 TW) from winds into the Ekman layer (Wang and Huang, 2004) and a significant amount of the total energy of 2 TW needed for maintaining the global ocean stratification (Munk and Wunsch, 1998; Wunsch and Ferrari, 2004). The energy of NIWs also penetrates the ocean interior, reinforcing the vertical shear and nourishing the ocean mixing (Alford and Gregg, 2001; Kunze et al., 1990; Munk and Wunsch, 1998; Sloyan and Rintoul, 2001). During extreme meteorological conditions such as tropical cyclones, the NIWs are significantly enhanced, and a series of ocean dynamic and thermodynamic responses can be triggered (Price, 1981), such as the enhancement of near-inertial currents characterized by opposite phases in the mixed layer and the thermocline (Zhang et al., 2016). Therefore, the NIWs are one of the most important forms of energy transport from the atmosphere to the ocean, an important component of the energy cascade in the ocean interior, and an important energy source for diapycnal mixing.

The NIWs have been captured in many *in-situ* observations. These waves and their interactions with the subtropical front were documented during FRONTS'80 (Kunze and Sanford, 1984).

Foundation item: The National Natural Science Foundation of China under contract Nos 42125601 and 42076001; the Scientific Research Fund of the Second Institute of Oceanography, Ministry of Natural Resources, under contract Nos HYGG2003 and QNYC2002; the project supported by the Southern Marine Science and Engineering Guangdong Laboratory (Zhuhai) under contract No. SML2021SP207; the Oceanic Interdisciplinary Program of Shanghai Jiao Tong University under contract No. SL2020MS032; the CEES Visiting Fellowship Program under contract No. CEESRS202001; the Innovation Group Project of Southern Marine Science and Engineering Guangdong Laboratory (Zhuhai) under contract No. 311021001.
*Corresponding author, E-mail: zhoulei1588@sjtu.edu.cn

Many progresses in the understanding of NIWs have been achieved as a result of the Ocean Storms Experiment (D'Asaro, 1995). Qi et al. (1995) estimated various properties of NIWs using data from the Ocean Storms Experiment, such as the response timescale, horizontal and vertical wavelengths, and group velocities. Particularly, they found a striking feature that the near-inertial responses below the mixed layer lagged those in the mixed layer by about a week (Levine and Zervakis, 1995). This feature was also captured by a mooring in the eastern Pacific as shown in Alford et al. (2012) and by the Electromagnetic Autonomous Profiling Explorer (EM-APEX) floats (Sanford et al., 2011). Upon the arrival of a tropical cyclone (TC), the NIWs in the upper layer are reinforced rapidly. However, the energy seems to be trapped in the upper boundary layer without shedding continuous beams into the deep ocean. Approximately, 70%–90% of NIW energy dissipates in the upper layer (Furuichi et al., 2008). Several days later, the high-mode NIWs with relatively small vertical wavelengths suddenly penetrate through the bottom of the upper layer and rapidly propagate downward. Due to the small vertical scale, the vertical shears and ocean mixing at the bottom of the boundary layer and below are greatly enhanced (Hebert and Moum, 1994; Silverthorne and Toole, 2009; van Haren and Gostiaux, 2012). In contrast, in many numerical simulations, the vertical propagation of NIWs is usually continuous and gradual even in a high-resolution model, which is a clear discrepancy from observations (Levine and Zervakis, 1995; Simmons and Alford, 2012). In addition, the simulated vertical shear due to NIWs around the bottom of the boundary layer is usually weaker than observations, which results in weaker mixing and biases in the simulated NIW decay (D'Asaro, 1985; D'Asaro et al., 1995; Simmons and Alford, 2012).

Since the NIWs are one of the major energy sources for ocean mixing (the other one is the internal tide; Munk and Wunsch, 1998), they play an important role in climate models. Nowadays, the horizontal model resolutions are high enough for resolving the NIWs. For example, Zhai et al. (2007) used a modified version of Modular Ocean Model (MOM) with a horizontal resolution of (1/12)°. However, since the vertical scale of high-mode NIWs is about 10–100 m (van Haren and Gostiaux, 2012), the vertical structure of NIWs can hardly be fully resolved in contemporary models. As a result, the decay of NIWs in the boundary layer and their energy propagation into the deep ocean are still challenges for the ocean general circulation models (OGCMs). In addition, the detailed mechanisms for NIW's penetration through the upper boundary layer and the consequent mixing are not well understood (Alford et al., 2016). Therefore, an appropriate parameterization for NIWs in an OGCM is desired. Jochum et al. (2013) proposed a parameterization (referred to as J13 scheme hereafter) for NIWs and applied it to the community climate system model, version 4 (CCSM4). The results showed that the mixing due to NIWs deepened the boundary layer. On the global scale, the adoption of the NIW parameterization had pronounced impacts on mean sea surface temperatures (SSTs), which were large enough to modulate the intertropical convergence zone (ITCZ), especially showing a major improvement in the chronic double-ITCZ bias that plagues the state-of-the-art climate models (MacKinnon et al., 2017). This parameterization is widely used. For example, the J13 scheme was adopted in an energetically consistent model developed by Olbers and Eden (2013). The J13 scheme was also examined as a major NIW parameterization by the Climate Process Team (MacKinnon et al., 2017). However, this scheme has not been compared with observations yet.

In this study, mooring observations were conducted in the South China Sea (SCS) in 2014 and Typhoon Kalmaegi was captured. Such observations provide a unique opportunity to examine the NIW parameterization during typhoon, such as the J13 scheme, and this is the motivation of this study. It is shown in the following analyses that there are three important differences between the J13 scheme and the observed NIWs:

(1) The observed NIWs are trapped in the upper boundary layer for about 3 d without significant penetration into the ocean interior.

(2) The observed NIWs remains pronounced below the boundary layer for about 10 d after the TC leaves the moorings and the NIWs diminish in the upper boundary layer.

(3) Diapycnal mixing associated with NIWs has two peaks in the vertical which is different from the single peak in the J13 scheme.

It is also shown below that these discrepancies cannot be removed merely by increasing the model resolution. Instead, a better parameterization for NIWs is still desired even for state-of-the-art climate models. Thus, the J13 scheme is modified based on *in-situ* observations during typhoon, and all above discrepancies are reduced. In this study, no numerical modellings are conducted. Instead, the observations are treated as model outputs and are used to examine the J13 scheme in each step.

In the following, Section 2 provides details of the observations. Section 3 introduces and compares the J13 scheme with observations. Section 4 proposes improvements to the NIW parameterization which can yield a better match with the observations. Section 5 presents the summary and discussion.

2 Data

In 2014, five buoys and four subsurface moorings were deployed at five stations in a cross shape from July to November in the SCS (Fig. 1). The locations are listed in Table 1. The array captured Typhoons Rammasun, Matmo, and Kalmaegi in 2014, but were also severely damaged by typhoon. Buoys #2 and #4 had complete records during Typhoon Kalmaegi (Zhang et al., 2016, 2018). There were no current data at Buoys #3 and #5, and no temperature and salinity at Buoy #1. Thus, only data from Buoys #2 and #4 are used in this study. The meteorological variables (wind speed, humidity, air temperature, precipitation, air pressure) were measured by an Airmar WS-200WX Weather Station

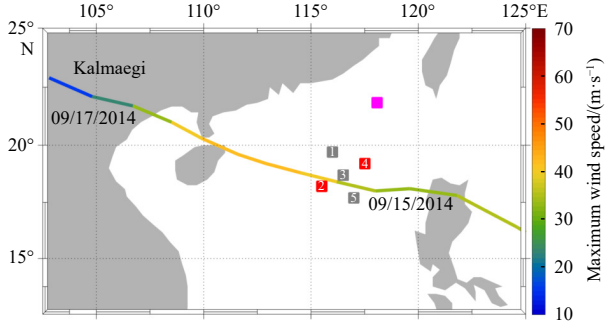

Fig. 1. Five buoys deployed in the South China Sea in 2014 and the trajectory of typhoon Kalmaegi. The locations of the buoys are listed in Table 1. Buoys #2 and #4 are used in this study and they are marked with red squares. Other three buoys (gray squares) were destroyed by the typhoon and the data were not complete. The purple square denotes the location of observations using the VMP-250 in 2019. The colors on the typhoon trajectory indicate the maximum wind speed.

Table 1. Locations of the buoys deployed in the South China Sea in 2014

Buoy ID	Latitude	Longitude
1	19.70°N	116.00°E
2	18.20°N	115.50°E
3	18.70°N	116.50°E
4	19.20°N	117.50°E
5	17.70°N	117.00°E

Note: The locations are also marked in Fig. 1.

Instrument (AirMar-200WX), which was deployed at 4 m above the sea surface. The sampling period was 10 min on Buoy #2 and 1 h on Buoy #4. The accuracy for wind speed is 0.5 m/s plus 10% of reading during low wind speeds (0–5 m/s) and 1 m/s plus 5% of reading during high wind speeds (5–40 m/s). For wind directions, the accuracy is 5° during low wind speeds (2–5 m/s) and 2° during high wind speeds (>5 m/s). The accuracy for the air temperature is 1.1°C and that for the barometric pressure is 1 mbar (1 hPa). The seawater temperature and conductivity were measured by fifteen SeaBird 37 sensors on each buoy. These sensors were deployed at depths of 0 m, 20 m, 40 m, 60 m, 80 m, 100 m, 120 m, 140 m, 170 m, 200 m, 240 m, 280 m, 320 m, 360 m, and 400 m. The sampling period was 2 min. The temperature accuracy was 2×10^{-3}°C and the electrical conductivity accuracy (for salinity) was 3×10^{-4} S/m. Ocean currents were observed by the Acoustic Doppler Current Profiler (ADCP). On Buoy #2 (#4), a 150 kHz (300 kHz) downward-looking ADCP was mounted at the surface and binned into an interval of 8 m (4 m) with the first bin at 14 m (8 m). The velocity accuracy for the 300 kHz ADCP was 0.5% of the water velocity relative to ADCP ± 0.5 cm/s (here written as 0.5% ± 0.5 cm/s), and the accuracy for the 150 kHz ADCP is 1% ± 0.5 cm/s.

In May 2019, a continuous 2-d microstructure observation experiment was conducted on the continental slope in the northeastern SCS at 21.8°N and 118°E, using a vertical microstructure profiler, the Light-Weight Coastal Vertical Profiler-250 (VMP-250; Rockland Scientific International, Victoria, Canada). Due to the VMP-250 cannot be performed during typhoon, only observations under normal weather conditions are available. The VMP-250 is equipped with two shear probes which measure the microscale velocity shear at a frequency of 512 Hz (Wolk et al., 2002). Based on these microscale shear data, the turbulent shear spectra are computed to estimate the turbulent kinetic energy dissipation rate ε. Using ε and buoyancy frequency N, the vertical turbulent eddy diffusivity can be estimated following the diffusivity model $\kappa=\frac{\Gamma\varepsilon}{N^2}$, where $\Gamma=0.2$ is the nominal flux coefficient (Osborn, 1980). Then the vertical structure of diffusivity is obtained, which is compared with the J13 scheme for the mixing intensity below the boundary layer.

Tropical cyclone tracks are obtained from the best track dataset of the China Meteorological Administration (http://tcdata.typhoon.org.cn; Ying et al., 2014).

3 Comparisons between observations and the J13 scheme

All components in the J13 scheme are examined with *in-situ* observations. In this study, the model simulations with and without the J13 scheme in an OGCM are not compared with the observations. This should be done in the future. But we believe a reasonable match of the NIW parameterization with observations (after possible improvement to the parameterization thereby) should be a prerequisite for a comprehensive evaluation of the influences of parameterization in an OGCM.

To facilitate the comparisons between observations and the parameterization, all variables (i.e., an arbitrary variable X) for observations carry a subscript "obs" (i.e., $X_{\rm obs}$) and the ones for parameterization carry a subscript "para" (i.e., $X_{\rm para}$). In addition, an arbitrary variable X that carries a subscript "1", "h" and "d" denotes the one at the sea surface, at the boundary layer depth, and below the boundary layer, respectively. All variables with a superscript n denote the ones without NIWs (obtained after a lowpass filtering with a cutoff period of 40 h), and the variables with a superscript i denote a near-inertial component. The important variables are listed in Table 2.

3.1 *Wind energy input into the ocean*

Following Jochum et al. (2013), the near-inertial energy from winds to the ocean is expressed as

$$E^i=\vec{u}^i\cdot\vec{\tau}, \tag{1}$$

where $\vec{u}^i=(u^i,v^i)$ is the near-inertial ocean current vector at the sea surface, u and v are the zonal and meridional velocities, respectively; and $\vec{\tau}=(\tau_x,\tau_y)$, τ_x and τ_y are zonal and meridional surface wind stress, respectively. They are estimated from the observations using the bulk formula, i.e., $\vec{\tau}=\rho_{\rm a}C_{\rm D}|\vec{u}_{10}|\vec{u}_{10}$, where $\rho_{\rm a}$=1.29 kg/m^3 is the air density, $C_{\rm D}$ is the drag coefficient, and $\vec{u}_{10}$ is the wind velocity at 10 m. $C_{\rm D}$ is taken from Li and Qian (1989),

Table 2. Definitions of key variables

Variable	Definition	Variable	Definition
u, v	zonal and meridional ocean current velocities in observations	$\varepsilon^i_{\rm para}$	energy dissipation due to NIWs in the boundary layer in the J13 scheme
$u^i_{\rm para}$, $v^i_{\rm para}$	near-inertial velocities in the J13 scheme	$\varepsilon^i_{\rm obs}$	energy dissipation due to NIWs in the boundary layer in observations
$u^i_{\rm obs}$, $v^i_{\rm obs}$	near-inertial velocities in observations	$\varepsilon^i_{\rm para_new}$	energy dissipation due to NIWs in the boundary layer in modified scheme
u^n_1, v^n_1	velocities without NIWs at the sea surface	$\varepsilon_{\rm para}$	near-inertial energy input available for mixing below the boundary layer in the J13 scheme
u^i_1, v^i_1	near-inertial velocities at the sea surface	$\varepsilon_{\rm obs}$	near-inertial energy input available for mixing below the boundary layer in observations
u^n_h, v^n_h	velocities without NIWs at the boundary layer depth	$\varepsilon_{\rm para_new}$	near-inertial energy input available for mixing below the boundary layer in modified scheme
u^i_h, v^i_h	near-inertial velocities at the boundary layer depth	$\kappa_{\rm para}$	diffusivity due to NIWs in the J13 scheme
$h_{\rm para}$	boundary layer depth in the J13 scheme	$\kappa_{\rm obs}$	diffusivity due to NIWs in observations
$h_{\rm obs}$	boundary layer depth in observations	$\kappa_{\rm para_new}$	diffusivity due to NIWs in modified scheme
$h_{\rm para_new}$	boundary layer depth in modified scheme		

$$C_{\mathrm{D}} \times 10^3 = \begin{cases} 0.85 & 0 \leqslant |\vec{V}| < 2\ \mathrm{m/s} \\ 0.85\ \text{to}\ 0.90 & 2 \leqslant |\vec{V}| < 6\ \mathrm{m/s} \\ 1.28\ \text{to}\ 2.00 & 6 \leqslant |\vec{V}| < 11\ \mathrm{m/s} \\ 2.39\ \text{to}\ 2.43 & 11 \leqslant |\vec{V}| < 18\ \mathrm{m/s} \\ 2.6 & |\vec{V}| \geqslant 18\ \mathrm{m/s} \end{cases}. \quad (2)$$

C_{D} takes the median value when the wind speed is in a certain range. $\vec{u}_{10}$ is calculated following the logarithmic law (Fleagle and Businger, 1980),

$$\vec{u}_{10} = \vec{u}_4 \frac{\ln(10/z_0)}{\ln(4/z_0)}, \quad (3)$$

where $\vec{u}_4$ is the observed wind speed at 4 m and z_0=2×10^{-4} m is the roughness length (Troen and Petersen, 1989).

From observations, $\vec{u}^i_{\mathrm{obs}}$ is obtained with a Butterworth bandpass filter between 0.7f and 1.3f, where f is the Coriolis parameter at the buoys' locations. For example, $\vec{u}^i_{\mathrm{obs}}$ at –22 m from Buoy #2 is shown in Figs 2a and b with red lines. In the J13 scheme, it is assumed that the NIWs dominate the temporal tendency of ocean velocities. Thus, $\vec{u}^i_{\mathrm{para}}$ can be estimated with the difference between two adjacent records and one has approximately as follows:

$$u^i_{\mathrm{para}}(t) \approx -\frac{1}{f}\frac{v(t) - v(t-\Delta t)}{\Delta t}, \quad (4a)$$

$$v^i_{\mathrm{para}}(t) \approx \frac{1}{f}\frac{u(t) - u(t-\Delta t)}{\Delta t}, \quad (4b)$$

where Δt is the time interval between two records, u and v are the total ocean current velocities in observations. The sampling period of pseudo-simulations (actual observations) is 3 min (Buoy #2 and Buoy #4) or 15 min (Mooring #2 and Mooring #4). When Δt is small, variabilities with high frequencies (higher than f) are energetic and diminish the near-inertial variabilities. Various running mean smoothing (every 1 h, 2 h, 3 h, 4 h, 6 h, 8 h, 12 h, and 24 h) are examined to suppress the high-frequency variabilities. It turns out that with a running mean of 12 h, $\vec{u}^i_{\mathrm{para}}$ (blue lines in Figs 2a and b) obtained from Eq. (4) has the best match with $\vec{u}^i_{\mathrm{obs}}$, especially after typhoon Kalmaegi from September 15 to 21 when the NIWs are strong near the surface. The vertical profiles of inertial zonal and meridional velocities at Buoy #2 are compared in Figs 2c and d. The consistency between the observations (colors in Figs 2c and d) and the parameterizations (contours in Figs 2c and d) is distinct. Therefore, the parameterization for $\vec{u}^i$ in the J13 scheme works well if an appropriate smoothing is applied to the model outputs.

For the energy input into the ocean, following Eq. (1), E^i_{obs} is calculated with $\vec{u}^i_{\mathrm{obs}} \cdot \vec{\tau}$ (red lines in Fig. 3). Similarly, E^i_{para} is estimated with $\vec{u}^i_{\mathrm{para}} \cdot \vec{\tau}$, where $\vec{u}^i_{\mathrm{para}}$ is obtained with Eq. (4) after a 12-h running mean (blue lines in Fig. 3). Since $\vec{u}^i_{\mathrm{para}}$ matches $\vec{u}^i_{\mathrm{obs}}$ (Fig. 2), especially during the typhoon period, E^i_{para} has a good agreement with E^i_{obs}. However, a caveat in the accuracy of Eq. (1) during typhoon is that the surface elevation can be much larger than 10 m and $\vec{u}_{10}$ can hardly be defined accurately. Moreover, the NIWs in the J13 scheme work well in the boundary layer, but the differences mainly reside in the phase lag between the NIWs in the boundary layer and those below the boundary layer. Therefore, a better parameterization scheme for NIWs is still

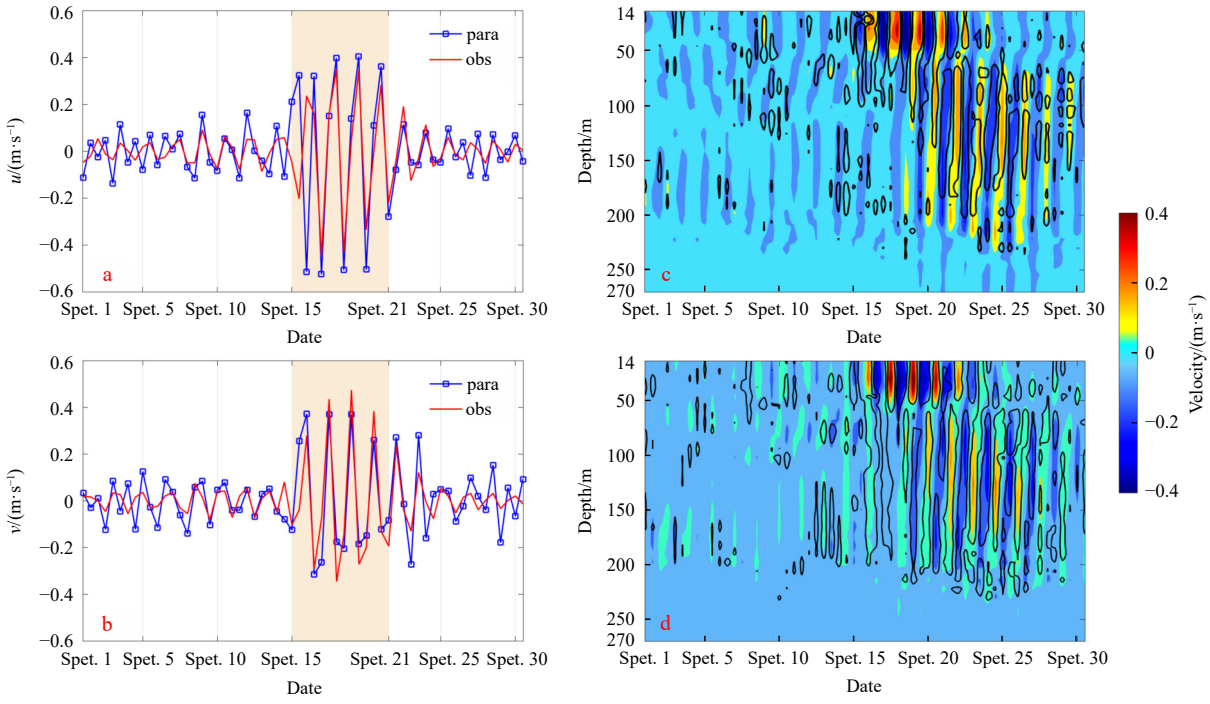

Fig. 2. The comparison of near-inertial velocities. In a, the red line shows u^i_{obs} at 22 m and Buoy #2, which is obtained with a Butterworth bandpass filter between 0.7f and 1.3f; the blue line shows the corresponding u^i_{para} obtained with Eq. (4a) after a 12-h running mean. In b, the red line and blue line are for v^i_{obs} and v^i_{para} at 22 m and Buoy #2. c shows the comparisons between u^i_{obs} (colors) and u^i_{para} (black contours) at Buoy #2. d is the same as c but for the comparisons between v^i_{obs} (colors) and v^i_{para} (black contours). The yellow shades in a and b are from September 15 to 21, when the wind speed is larger than 30 m/s and typhoon Kalmaegi had a direct impact on the buoy array. Para: parameterization, obs: observation.

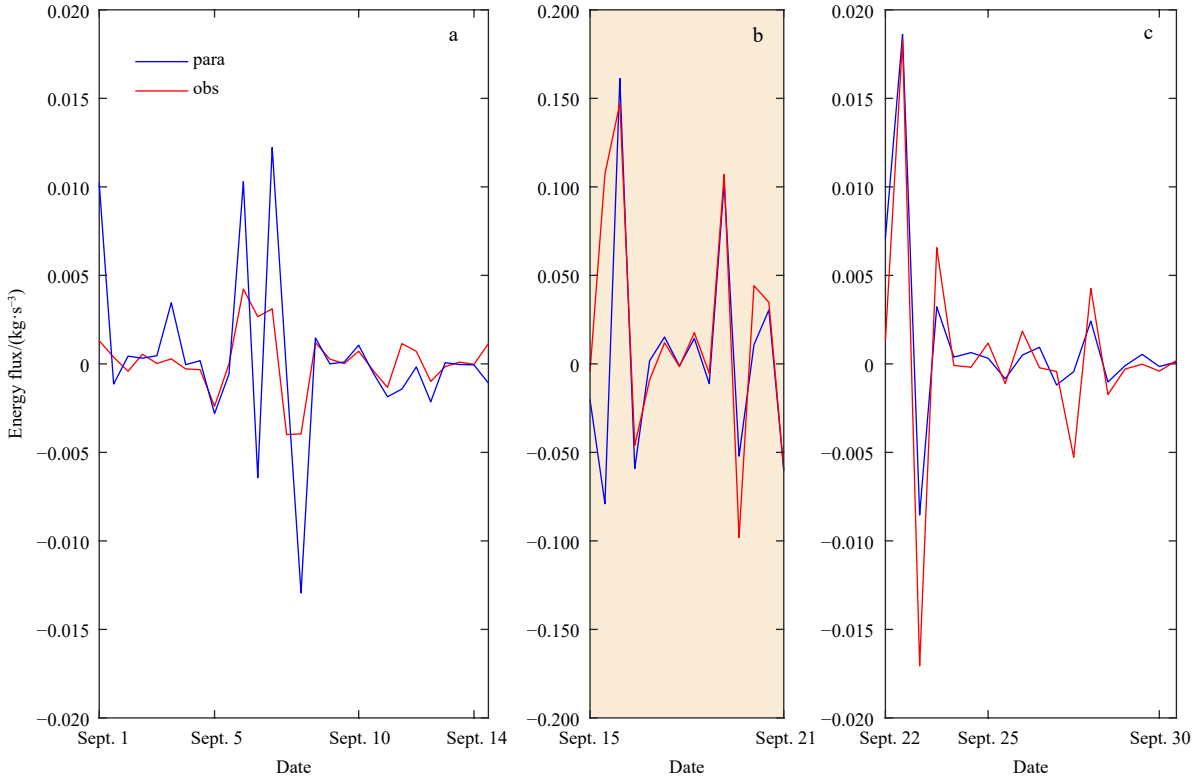

Fig. 3. Near-inertial energy input from winds into the ocean estimated with the observations ($E^i_{\rm obs}$=$\vec{u}^i_{\rm obs}\cdot\vec{\tau}$; red lines) and the J13 scheme ($E^i_{\rm para}$=$\vec{u}^i_{\rm para}\cdot\vec{\tau}$; blue lines). See the main text for details. All data are obtained from Buoy #2. Since the energy input is much larger during typhoon, the vertical scale for b is different from the vertical scales for a and c.

needed in high-resolution models.

3.2 *Boundary layer depth in the upper ocean*

The boundary layer is created by turbulent mixing through convective and wind-driven shear instabilities, Langmuir circulations, breaking waves, and the convergence of advected fronts (Ten Doeschate et al., 2017). Based on the K-profile parameterization (KPP; Large et al., 1994), the boundary layer is determined by the bulk Richardson number ($Ri_{\rm b}$), when $Ri_{\rm b}$ less than a critical value is dynamically unstable. Near the bottom of the boundary layer in the upper ocean, vertical shears are greatly enhanced due to high-mode NIWs (Alford et al., 2016). Thus, the boundary layer depth is critical for the enhanced ocean mixing caused by NIWs. From observations, the boundary layer depth $h_{\rm obs}$ is estimated based on the bulk Richardson number, following the classical KPP (Large et al., 1994), and $Ri_{\rm b}=\dfrac{(b_1-b_h)h}{(u_1-u_h)^2+(v_1-v_h)^2}$, where u and v are the total observed current velocities, b is the buoyancy. All variables with a subscript 1 denote the ones at the sea surface, and the subscript h denotes the boundary layer depth. All variables in this equation are estimated with observations. When the bulk Richardson number is smaller than a given critical value ($Ri_{\rm b}$), which is set to 0.3 in this study (Jochum et al., 2013), the shear instability is supposed to occur and the ocean mixing is reinforced. The vertical profiles of $|\vec{u}^i_{\rm obs}|$ at Buoy #2 in 2014 are shown in Fig. 4a (color shades), and the Brunt-Väisälä frequency (N^2) is shown in Fig. 4b. Due to the strong disturbance since September 15, the mixed layer in the upper 40 m is more uniform and N^2 becomes smaller than that before typhoon. Meanwhile, the stratification is reinforced around 60 m near the bottom of the boundary layer, which lasts from September 15 until early October. Since the ocean is well mixed and N^2 is small in the upper 40 m, the bulk Richardson number is calculated from 40 m to the deep ocean with each vertical profile of ocean currents and N^2. The depth at which the bulk Richardson number becomes smaller than 0.3 for the first time is chosen as the boundary layer depth ($h_{\rm obs}$). $h_{\rm obs}$ at Buoy #2 are shown in Fig. 4a with a blue line.

In the J13 scheme, the parameterization of boundary layer depth was modified from KPP (Large et al., 1994). In KPP with no NIWs, the boundary layer depth is parameterized as

$$h^n_{\rm KPP}=\frac{Ri_{\rm b}\left[\left(u^n_1-u^n_h\right)^2+\left(v^n_1-v^n_h\right)^2\right]}{b_1-b_h}, \tag{5}$$

where $Ri_{\rm b}$=0.3. All variables with a superscript n denote the ones without NIWs (obtained after a lowpass filtering with a cutoff period of 40 h). Note that, in the original KPP scheme (Large et al., 1994), ocean currents with all frequency components were considered. However, due to the low resolution of climate models at that time, the NIWs were actually much weaker than observations (Jochum et al., 2013). All variables in Eq. (5) are calculated with observations. For example, b_h is the buoyancy at the bottom of boundary layer from the observations. $h^n_{\rm KPP}$ at Buoy #2 is shown in Fig. 4a with a black line. It is much deeper than $h_{\rm obs}$ (blue line in Fig. 4a) during typhoon, which indicates that the velocity shear is underestimated due to the removal of NIWs (u^n and v^n, in which the NIWs are removed). Since the simulated near-inertial velocity shear is usually too weak in OGCMs, an extra velocity shear associated with NIWs is added to the KPP ($h^n_{\rm KPP}$) in the J13 scheme. Hence, the boundary layer depth is parameterized as

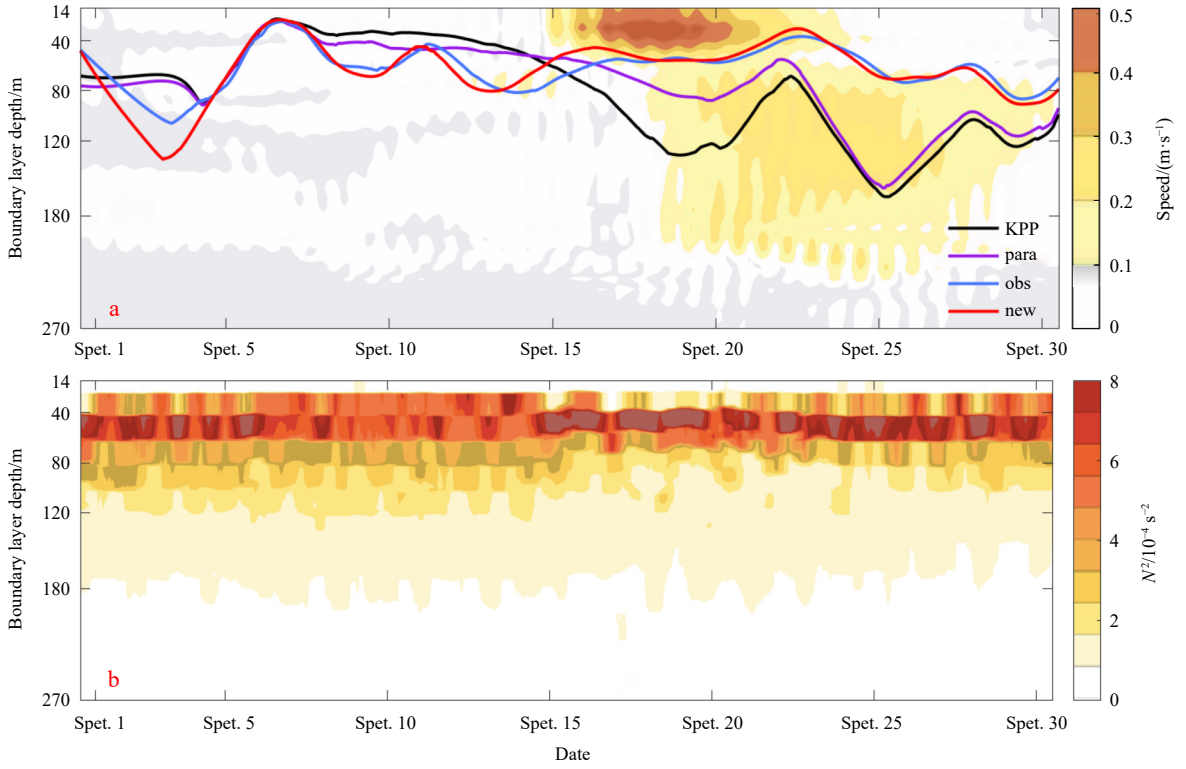

Fig. 4. The comparison of the boundary layer depth. a. Colors denote the speeds of near-inertial currents at Buoy #2, which are obtained with a Butterworth bandpass filter between 0.7*f* and 1.3*f*. The blue line shows the boundary layer depth h_{obs} obtained following the classical KPP scheme (Eq. (21) in Large et al. (1994)). The black line shows h^n_{KPP} in Eq. (5), the purple line shows h_{para} in Eq. (6), and the red line shows $h_{\mathrm{para_new}}$ in Eq. (11). b. The buoyancy frequency N^2 at Buoy #2. All data are smoothed with a 12-hour running mean. Para: parameterization, obs: observation.

$$h_{\mathrm{para}} = \frac{Ri_{\mathrm{b}}\left[\left(u_1^n + cu_1^i - u_h^n\right)^2 + \left(v_1^n + cv_1^i - v_h^n\right)^2 + \gamma\right]}{b_1 - b_h}, \tag{6}$$

where γ is the unresolved shear (Large et al., 1994), but it is ignored here; c=0.8, is the constant coefficient; the superscript i denotes a near-inertial component. h_{para} calculated at Buoy #2 is shown in Fig. 4a with a purple line. During Typhoon Kalmaegi from September 15 to 21, h_{para} is shallower than h^n_{KPP} (black line in Fig. 4a), due to the added near-inertial velocity shear (cu_1^i and cv_1^i in Eq. (6). However, h_{para} remains deeper than h_{obs} (blue line in Fig. 4a) during September 15–21, which implies that the vertical shear of NIWs during typhoon in the J13 scheme is still smaller than observations. In the wake of Typhoon Kalmaegi from September 22 to 30, h_{para} is comparable with h^n_{KPP}, since near-inertial velocities in the upper layer (u_1^i and v_1^i) become very weak (colors in Fig. 4a). Meanwhile, both h_{para} and h^n_{KPP} are still significantly deeper than h_{obs}, which indicates again that vertical velocity shear in the J13 scheme is much weaker than observations and the boundary layer depth in the J13 scheme tends to be too deep during typhoon.

3.3 *Near-inertial energy flux through the boundary layer*

The NIWs are an efficient way for wind energy to propagate into the ocean interior. After penetrating the upper boundary layer, the near-inertial energy can either spread to remote regions or dissipate locally, and the latter is critical for the enhancement of local mixing.

In the J13 scheme, the near-inertial energy input available for mixing (ε) below the boundary layer is estimated as

$$\varepsilon_{\mathrm{para}} = \varepsilon^i_{\mathrm{para}}\left(1 - b_{\mathrm{f}}\right) l_{\mathrm{f}}, \tag{7}$$

where $\varepsilon^i_{\mathrm{para}}$ is the near-inertial energy entering the boundary layer from winds; b_{f} = 0.7 denotes the fraction of near-inertial energy dissipated in the upper boundary layer (Alford and Whitmont, 2007); l_{f} = 0.5 represents that half near-inertial energy dissipates locally beneath the boundary layer (Furuichi et al., 2008). $\varepsilon^i_{\mathrm{para}}$ in the upper boundary layer is estimated based on the changes of total kinetic energy between two records, i.e.,

$$\varepsilon^i_{\mathrm{para}} = \alpha \cdot \Delta K_h = \alpha \frac{\left|K_h\left(t\right) - K_h\left(t - \Delta t\right)\right|}{\Delta t}, \tag{8}$$

where $K_h = \int_0^h \frac{\rho_0}{2}\left(u^2 + v^2\right) \mathrm{d}z$ and $\alpha = 0.05$ is a scaling factor. $\varepsilon^i_{\mathrm{para}}$ at Buoy #2 is shown in Fig. 5a with a blue line. The change of near-inertial kinetic energy in the boundary layer (K^i_h) between two records is assumed to be the dissipation of near-inertial energy, and $K^i_h = \int_0^h \frac{\rho_0}{2}\left(u^{i2}_{\mathrm{obs}} + v^{i2}_{\mathrm{obs}}\right) \mathrm{d}z$. Therefore, $\varepsilon^i_{\mathrm{obs}}$ is estimated with $\Delta K^i_h = \frac{\left|K^i_h(t) - K^i_h(t - \Delta t)\right|}{\Delta t}$ and it is shown in Fig. 5a with a red line.

Before the arrival of Typhoon Kalmaegi on September 14 and after the passing of the typhoon on September 24, $\varepsilon^i_{\mathrm{para}}$ in the J13 scheme is generally comparable with $\varepsilon^i_{\mathrm{obs}}$ (Fig. 5a). However, during typhoon, $\varepsilon^i_{\mathrm{para}}$ is much smaller than $\varepsilon^i_{\mathrm{obs}}$, which implies that the NIWs account for more energy dissipation than what is assumed in the J13 scheme. The ratio $\alpha' = \Delta K^i_h / \Delta K_h$ is shown in

Fig. 5b, which represents the same thing and could be compared with α. Over the typhoon period from September 14 to 24, α' is much larger than 0.05, which is the assumed value for the ratio α in the J13 scheme. The maximum of α' is about 0.6, which indicates that about 60% energy dissipation in the upper boundary layer is attributable to NIWs during Typhoon Kalmaegi.

Below the boundary layer, the energy dissipation due to NIWs ($\varepsilon_{\rm obs}$) is estimated by $\varepsilon_{\rm obs}=l_{\rm f}\times\frac{\left|K_d^i(t)-K_d^i(t-\Delta t)\right|}{\Delta t}$ and $K_d^i=\int_h^d\frac{\rho_0}{2}\left(u_{\rm obs}^{i2}+v_{\rm obs}^{i2}\right)\mathrm{d}z$, where h is the boundary layer depth and d=180 m is the depth below which NIWs are very weak (Fig. 4a). $\varepsilon_{\rm obs}$ and $\varepsilon_{\rm para}$ (Eq. (7)) are shown in Fig. 5c. Before September 15 when Typhoon Kalmaegi hits the moorings, $\varepsilon_{\rm obs}$ and $\varepsilon_{\rm para}$ are similar to each other. Under the influence of the typhoon, both $\varepsilon_{\rm obs}$ and $\varepsilon_{\rm para}$ increase before September 18, while the former increases much faster than the latter. The small $\varepsilon_{\rm para}$ is mainly attributable to small $\varepsilon_{\rm para}^i$ in the upper boundary layer (Eq. (7)). After September 18, due to the persistence of large NIWs below the boundary layer (colors in Fig. 4a and more discussion in Section 4), $\varepsilon_{\rm obs}$ remains large until early October. In contrast, $\varepsilon_{\rm para}$ reduces after September 18 along with the decrease of near-inertial velocities in the upper boundary layer. After September 21 when Typhoon Kalmaegi leaves the moorings and the near-inertial velocities become small in the upper layer, $\varepsilon_{\rm para}$ decreases significantly to a level which is comparable with the dissipation before typhoon. Therefore, the large energy dissipation in the wake of the typhoon (after September 18) is missing in the J13 scheme. Such discrepancy is reduced with the modification to the J13 scheme in Section 4.

3.4 *Diffusivity due to near-inertial waves*

According to the J13 scheme, below the boundary layer, diffusivity that is caused by the downward-propagating NIWs is computed as

$$\kappa_{\rm para}=\Gamma\frac{\varepsilon_{\rm para}}{\rho_h N_h^2}F(z)\,, \tag{9}$$

where Γ=0.2 is the mixing coefficient, and $F(z)$ is a vertical structure function,

$$F(z)=\frac{\mathrm{e}^{(z-h)/\zeta}}{\zeta(1-\mathrm{e}^{-h/\zeta})}, \tag{10}$$

where the vertical scale ζ=2 000 m and h is the boundary layer depth in the J13 scheme (Eq. (6)). All variables with a subscript h denote the ones at the bottom of the boundary layer. Note that $\varepsilon_{\rm para}$ is a parameterization for the energy dissipation beneath the boundary layer, and the vertical structure of $\kappa_{\rm para}$ is determined by $F(z)$. For observations, the diffusivity is calculated with $\kappa_{\rm obs}=\Gamma\frac{\varepsilon_{\rm obs}(z)}{\rho N^2}$, in which the vertical structure of $\kappa_{\rm obs}$ is mainly determined by $\varepsilon_{\rm obs}(z)$ and N^2.

During Typhoon Kalmaegi, $\kappa_{\rm obs}$ (Fig. 6a) is pronounced in the

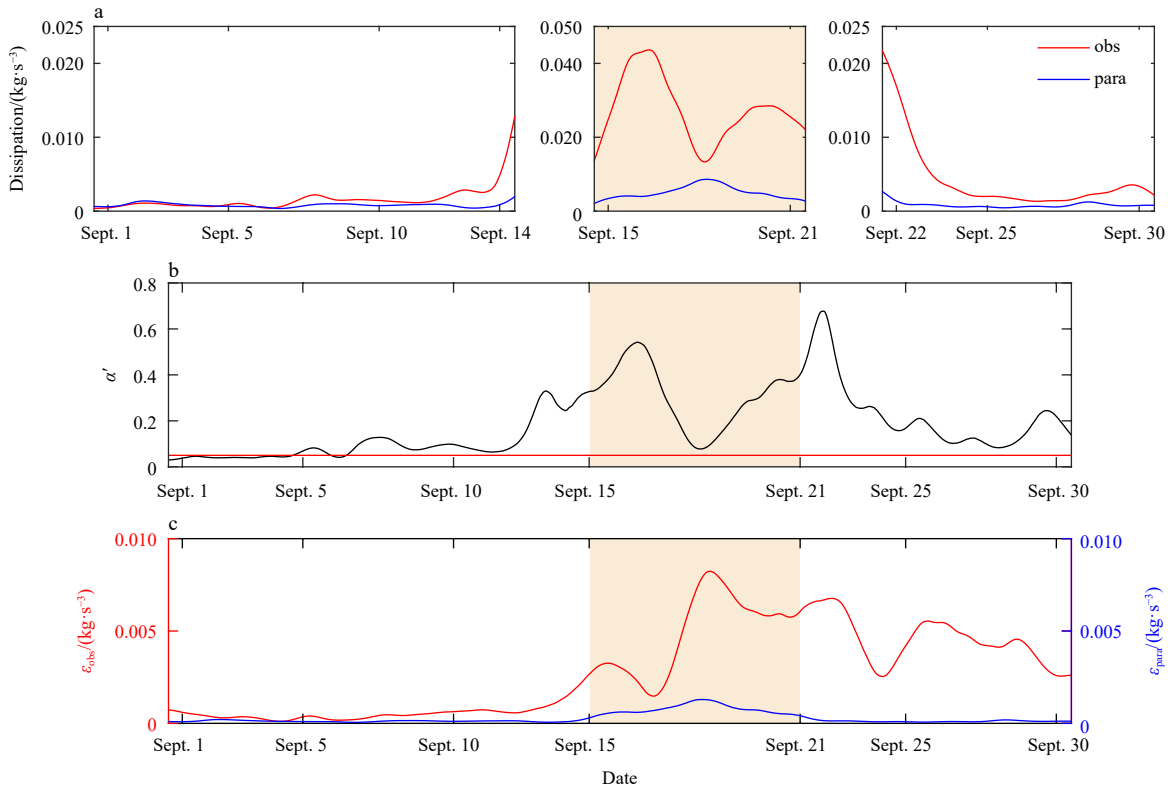

Fig. 5. The comparison of near-inertial energy dissipation. a. Near-inertial energy dissipation in the upper boundary layer estimated with observations ($\varepsilon_{\rm obs}^i$, red line) and with the J13 scheme ($\varepsilon_{\rm para}^i$, blue line) at Buoy #2. b. $\alpha'=\Delta K_h^i/\Delta K_h$, which indicates the ratio between the energy dissipation associated with the NIWs and the total energy dissipation in the upper boundary layer; the red line shows the ratio of 0.05, which is used in the J13 scheme. c. Near-inertial energy dissipation below the upper boundary layer estimated with observations ($\varepsilon_{\rm obs}$, red line) and with the J13 scheme ($\varepsilon_{\rm para}$, blue line) at Buoy #2. See the main text for the detailed methods to estimate the energy dissipation.

upper boundary layer from September 14 to 24, which is consistent with the energy dissipation shown in Figs 5a and c. The enhancement of κ_{obs} below the boundary layer occurs several days after the arrival of Typhoon Kalmaegi. However, the large κ_{obs} lasts until early October, which is much longer than it is in the upper boundary layer. In the J13 scheme, the temporal variation of κ_{para} depends on that of ε_{para} (blue line in Fig. 6b), and the vertical structure of κ_{para} depends on $F(z)$ which is shown in Fig. 6c. Due to the small energy dissipation associated with NIWs (Fig. 5c), κ_{para} is generally smaller than κ_{obs}. Moreover, since $F(z)$ reaches maximum at the bottom of the boundary layer, κ_{para} also reaches the maximum therein, which does not agree with observations (Fig. 6a). In addition, $F(z)$ does not have a large enough variability in the vertical. As a result, the vertical profiles of κ_{para} are more uniform than those of κ_{obs}. $F(z)$ is modified in Section 4 and the vertical structure is improved, compared with the observations.

4 Modifications to the NIW parameterization

With the increase of horizontal spatial resolutions in climate models, the simulation of NIWs in the upper boundary layer has been greatly improved. For example, near-inertial velocities were largely reproduced by Simmons and Alford (2012) using a nominal horizontal resolution of (1/8)° in both latitude and longitude. Therefore, the parameterization for near-inertial currents in the upper layer works well (Fig. 2), and it may seem not necessary to parameterize the near-inertial horizontal velocities in high-resolution climate models. However, the comparisons between the J13 scheme and the observations unveil some important discrepancies near and beneath the upper boundary layer, which require a better NIW parameterization.

4.1 *Boundary layer depth*

As shown in Fig. 4a, the boundary layer thickness (h_{para},

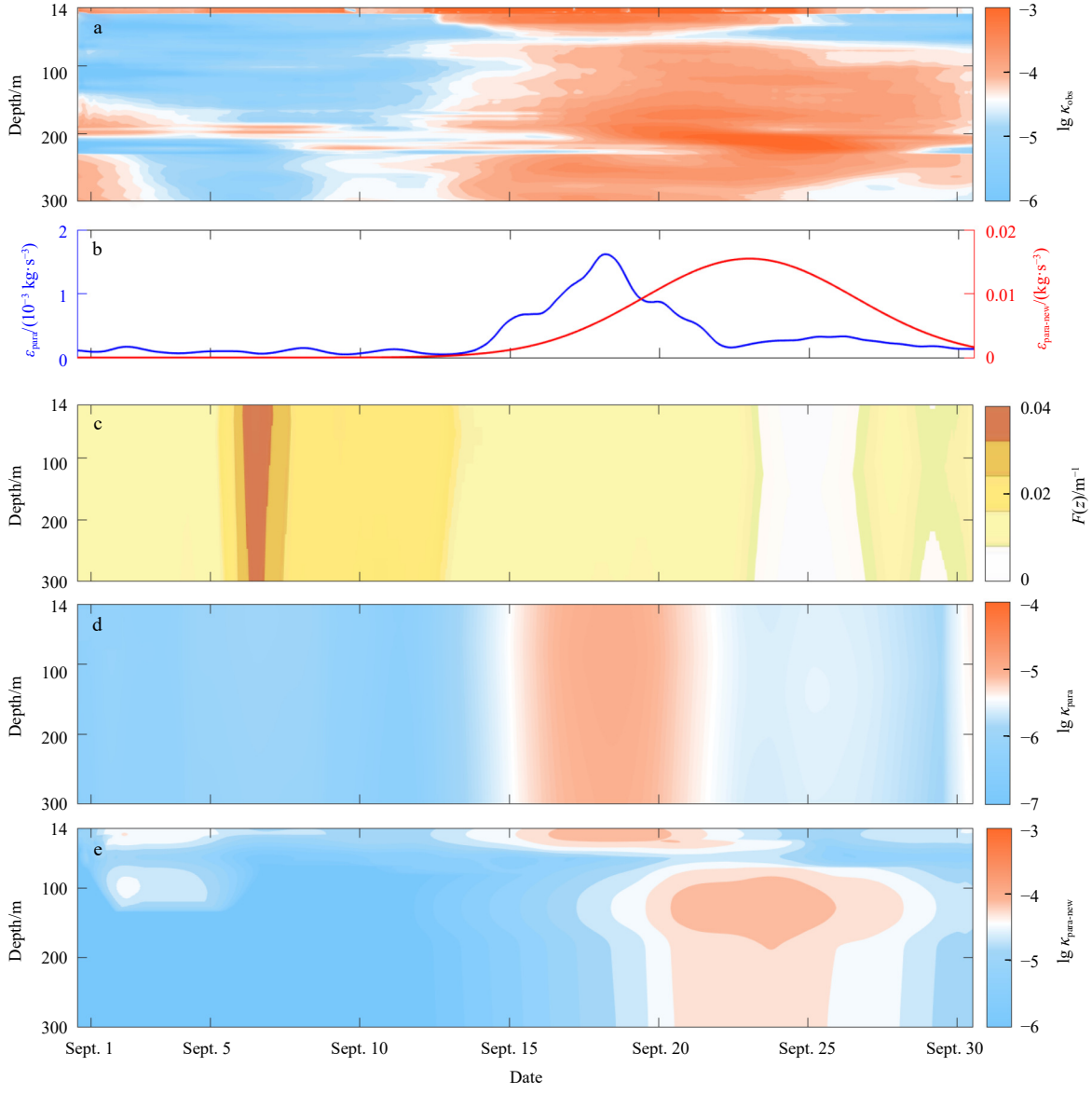

Fig. 6. The comparison of diffusivities. a. Vertical profiles of $\lg \kappa_{obs}$ at Buoy #2, where $\kappa_{obs} = \Gamma \frac{\varepsilon_{obs}(z)}{\rho N^2}$ is the diffusivity. b. ε_{para} (blue line) in Eq. (7) and ε_{para_new} (red line) in Eq. (12) at Buoy #2. c. Vertical profiles of $F(z)$ at Buoy #2. The boundary layer depth (h) in $F(z)$ is set to h_{para} (Eq. (6) and purple line in Fig. 4a). d. Vertical profiles of $\lg \kappa_{para}$. e. Vertical profiles of $\lg \kappa_{para_new}$. The unit for all diffusivities is m^2 /s.

purple line) is deeper than the observations (h_{obs}, blue line), since the vertical shear of NIWs in the J13 scheme is too weak, especially after September 21 when the near-inertial kinetic energy decays in the boundary layer. The J13 scheme assumed that the near-inertial velocity at the boundary layer depth could be neglected. However, the observations suggest otherwise (Fig. 4a). Therefore, the boundary layer depth can be modified as

$$h_{\text{para_new}} = \frac{Ri_{\text{b}}\left[\left(u_1^n + c_{\text{new}}u_1^i - u_h^n - c_{\text{new}}u_h^i\right)^2 + \left(v_1^n + c_{\text{new}}v_1^i - v_h^n - c_{\text{new}}v_h^i\right)^2\right]}{b_1 - b_h}, \tag{11}$$

where u_h^i and v_h^i are the near-inertial velocities at the bottom of the boundary layer, and all other variables carry the same meanings as in Eq. (6). The constant coefficient c_{new} in Eq. (11) has the same meaning as the coefficient c in the J13 scheme (Eq. (6)). However, the best fit to observations can be achieved when c_{new}=2.6 (red line in Fig. 4a), rather than c=0.8 in the J13 scheme (Eq. (6)). Due to the enhanced vertical shear of NIWs in Eq. (11), $h_{\text{para_new}}$ (red line in Fig. 4a) is more consistent with h_{obs} (blue line in Fig. 4a), especially in the wake of Typhoon Kalmaegi from September 22 to 30.

Meanwhile, the KPP (Large et al., 1994) is an important basis for the J13 scheme. The observed boundary layer thickness in a numerical study by Large and Grawford (1995) was well reproduced, which adopted the KPP and a vertical resolution of 2 m. However, the vertical resolution in observations is about 20 m, and in this way, an insufficient vertical resolution may also be the reason for the deeper boundary layer depth. Overall, the empirical coefficient c (also c_{new}) depends on the vertical resolutions in observations and models. More examinations and calibrations should be conducted to c_{new} in the future.

4.2 *Phase lag of NIWs in and below the boundary layer*

During typhoon, there is a clear phase lag between the enhancement of NIWs in the boundary layer and those below the boundary layer. As shown with colors in Fig. 4a, when Typhoon Kalmaegi reached the buoy array on September 15, the near-inertial kinetic energy was reinforced rapidly. The wind speed of Typhoon Kalmaegi was about 30 m/s around the buoy array. Its impact on the upper layer lasted for about 7 d until September 21. However, the NIWs below the boundary layer were not enhanced immediately along with the arrival of Typhoon Kalmaegi. Instead, for 3 d from September 15 to 17, the NIWs were trapped in the upper boundary layer and almost no near-inertial energy penetrated the bottom of the boundary layer. On September 18, the near-inertial energy suddenly broke into the ocean interior. According to the linear internal wave theory (Pedlowsky and Miles, 2004), the downward group velocity of near-inertial internal waves is about 2.04×10^{-4} m/s and it takes about 7.9 d to reach 200 m. However, as shown in Fig. 4a, after September 18, the vertical spread of NIWs in upper 200 m was too fast to be clearly resolved in the observations with a sampling period of 3 min. Such a feature was also captured by Hebert and Moum (1994). However, in high-resolution simulations, near-inertial energy propagates downward following the ray paths of theoretical near-inertial gravity waves, which is smooth and gradual from the sea surface to the ocean interior. Therefore, the fast vertical downward propagation of NIWs cannot be resolved even in modern high-resolution models. In the J13 scheme, the near-inertial energy is solely determined by the surface wind stress. As a result, the responses below the boundary layer are in high consistency with surface winds, which is different from observations.

In addition, the energy partition in the vertical after it enters the ocean from typhoon is re-examined between the J13 scheme and the observations. As discussed in Section 3.3, the scaling factor α=0.05 (red dashed line in Fig. 5b) in $\varepsilon_{\text{para}}^i$ (Eq. (8)) is significantly smaller than it should be in nature (α_{new} = 0.35 is the average of α' (black line in Fig. 5b) during the typhoon period from September 14 to 30), which indicates that the near-inertial energy carries more weight in the total kinetical energy during typhoon. Furthermore, Alford et al. (2012) showed that up to 50% of the NIW energy could escape the boundary layer and spread into the ocean interior, which leads to a reduction of b_{f}=0.7 in the J13 scheme (Eq. (7)) to $b_{\text{f}_{\text{new}}}$=0.5 . As a result, the near-inertial energy and associated dissipation below the boundary layer is enhanced. This is consistent with the evidence that ε_{obs} (red line in Fig. 5c) is much larger than $\varepsilon_{\text{para}}$ (blue line in Fig. 5c) in the J13 scheme during typhoon.

The phase shift shown in Fig. 6 is also considered for the modification. Although the mechanisms for the trapping of NIWs in the upper boundary layer and the fast spread of NIWs in the ocean interior are still open questions, a modification to the J13 scheme can reproduce the phase lag of NIWs in and below vthe boundary layer by introducing a factor of $\mathrm{e}^{-\left(\frac{t-t_0}{\tau}\right)^2}$, where t_0 is the time when dissipation reaches the maximum, and τ is a timescale for the decay of near-inertial energy below the boundary layer. Being estimated with observations during Typhoon Kalmaegi in the SCS, t_0 is seven days and τ is five days, and they are consistent with the timescales estimated in Chen et al. (2013) and Park et al. (2009).

Overall, the parameterization of the near-inertial energy dissipation below the boundary layer can be modified as follows (corresponding to Eq. (7)):

$$\varepsilon_{\text{para_new}} = \varepsilon_{\text{para_new}}^i \times \left(1 - b_{\text{f}_{\text{new}}}\right) \times l_{\text{f}} \times \mathrm{e}^{-\left(\frac{t-t_0}{\tau}\right)^2}, \tag{12}$$

where $\varepsilon_{\text{para_new}}^i = \alpha_{\text{new}} \cdot \Delta K_h$ (corresponding to Eq. (8)). Meanwhile, $\varepsilon_{\text{para_new}}$ is shown in Fig. 6b with a red line, and the phase shift from $\varepsilon_{\text{para}}$ (blue line in Fig. 6b) is distinct.

4.3 *Vertical profile of diffusivity*

In the J13 scheme, the diapycnal mixing is assumed to be enhanced due to strong vertical shear associated with NIWs (i.e., the bulk Richardson number reaches 0.3) near the bottom of the upper boundary layer. Then the diffusivity decreases both upward and downward following the vertical structure function $F(z)$. However, in observations, there are two peaks of κ_{obs} in the vertical (Fig. 6a). One peak is in the boundary layer, which is attributable to the direct stirring by surface winds. The other peak is well below the boundary layer bottom. In fact, during Typhoon Kalmaegi, κ_{obs} is relatively small around the bottom of the boundary layer (~60 m; blue line in Fig. 4a), probably due to the increase of N^2 (Fig. 4b) at that depth. Therefore, the vertical structure of κ_{obs} is not reasonably represented by $F(z)$. In 2019, the fine-structure observations were conducted in the SCS (purple square in Fig. 1), and nine casts are shown in Fig. 7. The peaks below the bottom of the boundary layer are obvious in

both the energy dissipation rate (black lines in Fig. 7) and the diffusivity (red lines in Fig. 7), although the specific depth changes. These peaks cannot be simply explained by the weak stratification since the stratification reduces gradually and almost monotonically below the boundary layer (not shown). The VMP-250 casts were not obtained during typhoon, since the microstructure observations cannot be performed manually during typhoon. It is hardly possible to separate the influences of NIWs from the fine-scale observations using VMP-250 in Fig. 7, either. However, the large diffusivities (κ_{obs}) are discernible below the boundary layer in Fig. 6a during Typhoon Kalmaegi, as estimated from the vertical shears of the NIWs. The similarity between the vertical structure of VMP-250 profiles and the estimated ones in Fig. 6a implies that the peak of the enhanced diapycnal mixing during typhoon should be well below, rather than near, the bottom of the boundary layer. Therefore, it is reasonable to assume that the enhanced diapycnal mixing due to NIWs has a second peak below the upper boundary layer, which is not captured in the J13 scheme.

A modification to the vertical structure function $F(z)$ in the J13 scheme is proposed as

$$F_{\mathrm{new}}(z) = \frac{\mathrm{e}^{(z-h_1)/\zeta}}{\zeta(1-\mathrm{e}^{-h_2/\zeta})}, \tag{13}$$

where h_1 and h_2 denote the center depths for the enhanced ocean

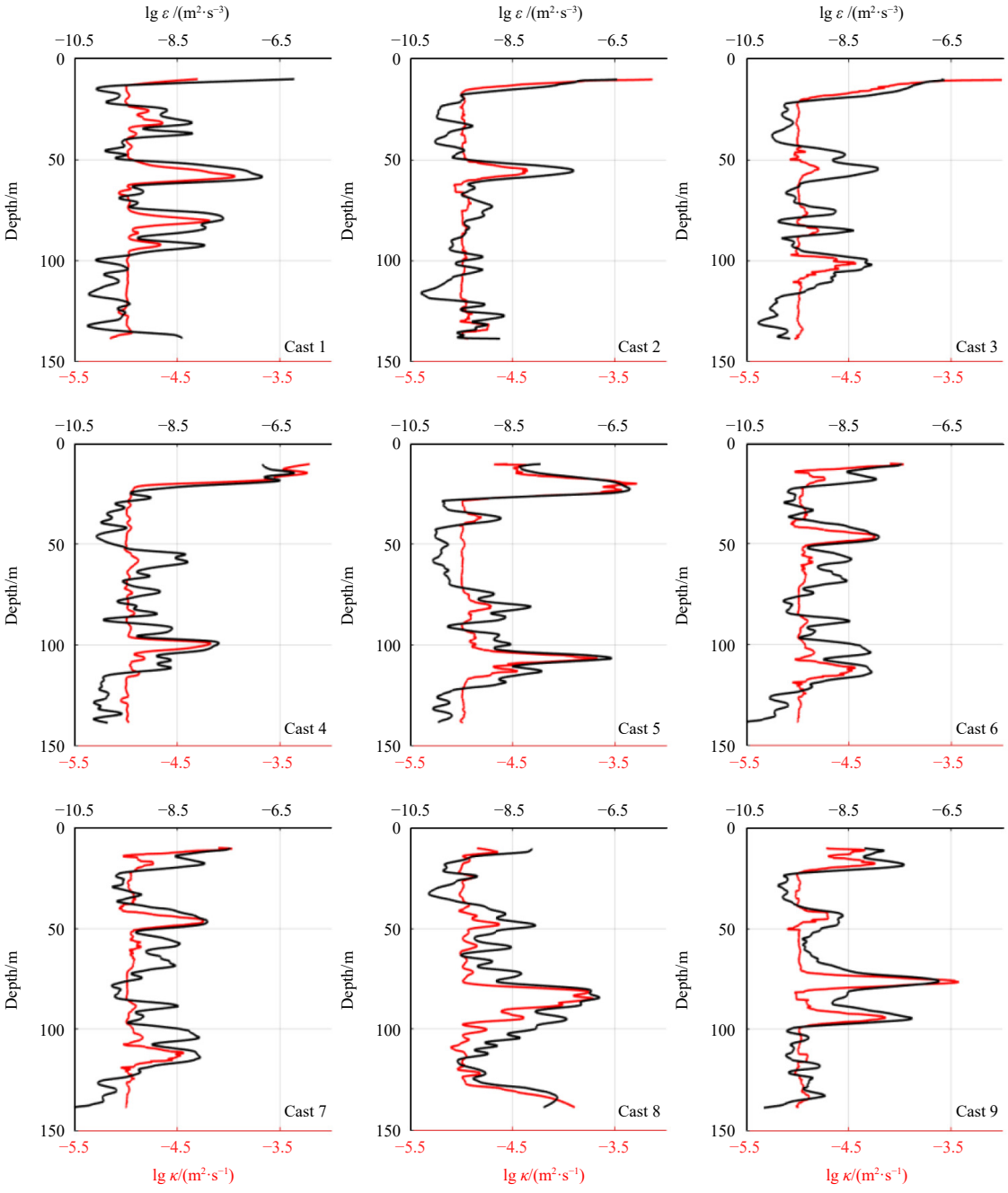

Fig. 7. $\lg\varepsilon$ and $\lg\kappa$ of nine casts. Black lines show $\lg\varepsilon$, where ε is the turbulent kinetic energy dissipation rate and is computed by the shear spectra that are observed by the VMP-250 in the SCS in 2019. Red lines show corresponding $\lg\kappa$, where $\kappa = \frac{\Gamma\varepsilon}{N^2}$ is the diffusivities.

mixing in and below the boundary layer, rather than a uniform boundary layer depth h in Eq. (10); all other variables carry the same meanings as in Eq. (10). The vertical structure function $F_{\text{new}}(z)$ is shown in Fig. 8a with a blue line and the time-average $F(z)$ is shown in Fig. 8a with a black line. Adopting the modified parameterization for near-inertial energy dissipation and the vertical structure function, the parameterization for diffusivity is written as $\kappa_{\text{para_new}} = \Gamma \frac{\varepsilon_{\text{para_new}}}{\rho_h N_h^2} F_{\text{new}}(z)$. The results during Typhoon Kalmaegi are shown in Fig. 6e. For the best fit between the parameterization and the observations, h_1 is 28 m and h_2 is 118 m. With the modified structure function $F_{\text{new}}(z)$ and dissipation $\varepsilon_{\text{para_new}}$ below the boundary layer, the diapycnal mixing, which is the goal of a NIW parameterization, is improved. The new structure function $F_{\text{new}}(z)$ captures two peaks of dissipation and diffusivity in the vertical, and the new dissipation below the boundary layer ($\varepsilon_{\text{para_new}}$) reproduces the time lag in the NIWs above and below the boundary layer depth. Therefore, the discrepancies in the temporal and vertical structures of diapycnal mixing between the modified version and observations are reduced.

Since the J13 scheme is designed for climate models, the mean diffusivity over a long time is also important. In Fig. 8b, the mean diffusivities obtained with different methods during the typhoon period from September 14 to 30 are compared. The red line is from the observations. The black line is obtained with the original J13 scheme. The variation of the black line is not discernible, since the values are too small compared with the observations. After the modification, the vertical profile of diffusivity is represented with the blue line in Fig. 8b. Obviously, the modified scheme has a much better rendition of diffusivity.

5 Discussion and conclusions

The NIWs are ubiquitous in the global ocean and contribute greatly to diapycnal mixing. Due to insufficient understanding of the detailed mechanisms and the limitation of vertical resolution in models, an appropriate parameterization for NIWs and associated diapycnal mixing are still inevitable in contemporary ocean and coupled climate models. A parameterization of NIWs was proposed in Jochum et al. (2013) (the J13 scheme), which consists of five major components: (1) near-inertial ocean currents, (2) near-inertial energy input from winds, (3) the upper boundary layer depth, (4) energy dissipation beneath the boundary layer, and (5) diapycnal diffusivity due to NIWs. All components in the J13 scheme are compared with observations in the SCS, especially the *in-situ* data obtained during Typhoon Kalmaegi in 2014. The near-inertial velocities in the upper layer and the wind energy input into the ocean obtained from the J13 scheme are comparable with observations. However, the parameterized boundary layer thickness is deeper than observations, which indicates that the vertical velocity shear is still weak in the J13 scheme. As a result, the energy diffusion at the bottom of the boundary layer is

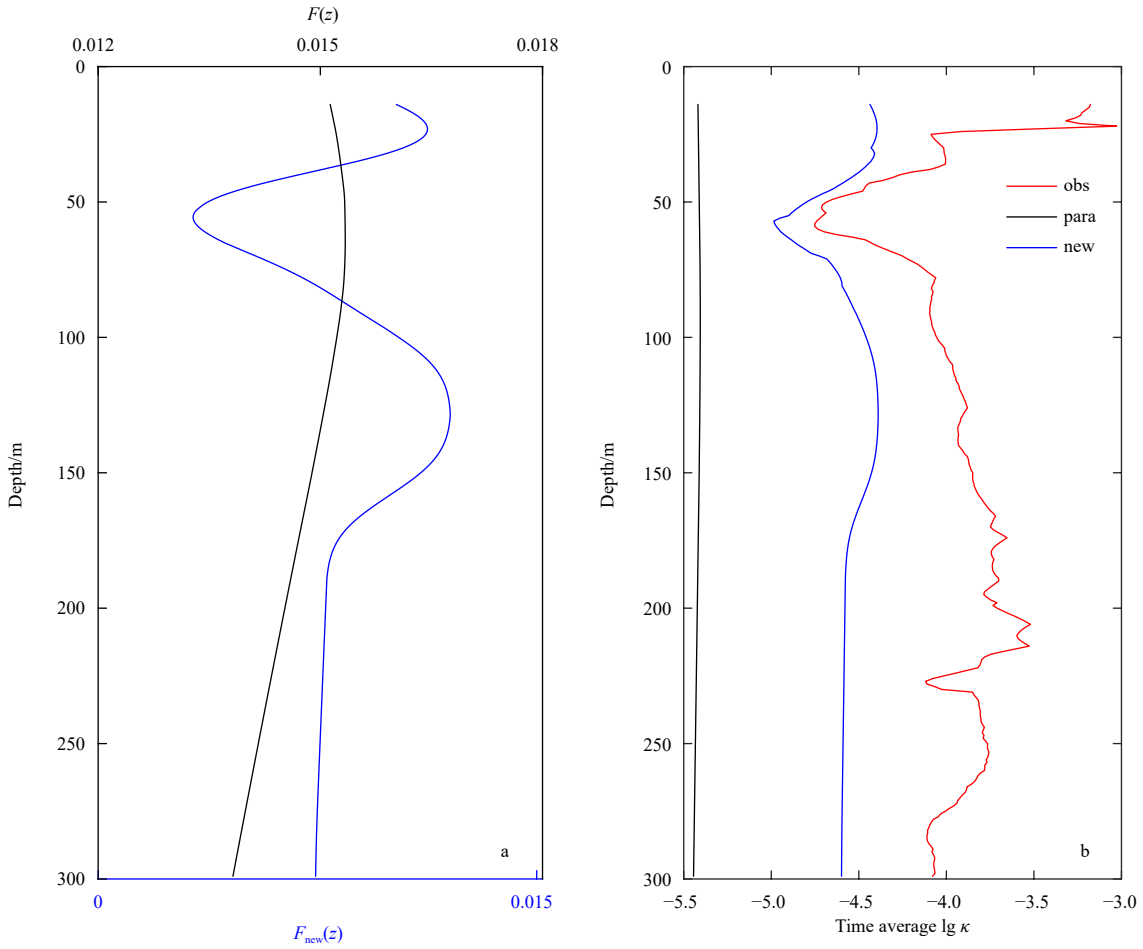

Fig. 8. The comparison of the vertical structure function and the mean diffusivity. a. Vertical profiles of $F_{\text{new}}(z)$ (blue line) and $F(z)$ (black line) at Buoy #2. b. Time average $\lg \kappa_{\text{obs}}$ (red line), $\lg \kappa_{\text{para}}$ (black line) and $\lg \kappa_{\text{para_new}}$ (blue line) from September 14 to 30. The unit for all diffusivities is m^2/s.

also weaker in the J13 scheme than in observations. The diapycnal mixing is the goal of a NIW parameterization. There are discrepancies in the spatial and the vertical structures of diapycnal mixing between the J13 scheme and observations. The NIWs are rapidly reinforced upon the arrival of typhoon. However, the near-inertial energy is trapped in the upper layer for the first several days (e.g., September 15 to 17 for Typhoon Kalmaegi). When NIWs penetrate through the upper layer, the near-inertial energy propagates very fast in the vertical and lasts longer in the ocean interior than it does within the upper layer. Therefore, the enhanced ocean mixing due to NIWs persists for more than 10 d after the typhoon passes. In contrast, the parameterized diapycnal mixing in the J13 scheme is bounded to the surface wind stress, thus κ_{para} in the whole water column gets enhanced when the typhoon arrives and diminishes when typhoon leaves. In the vertical, the large diapycnal mixing is assumed to occur at the bottom of the boundary layer and decreases with the increase of depth (denoted with a structure function $F(z)$). However, in observations, the ocean mixing reaches the maximum below the bottom of the boundary layer, which is significantly deeper than the parameterization.

All above discrepancies are significantly reduced with the modifications to the original J13 scheme that we propose in this study. Particularly, the boundary layer depth decreases, since the near-inertial velocities at the bottom of the boundary layer are considered and the vertical shear is reinforced. The phase lag of the NIWs above and below the bottom of the boundary layer is reproduced by introducing a new expression for energy dissipation (Eq. (12)). As a result, the prolonged influence of typhoon-induced NIWs in the ocean interior is captured. The vertical function $F(z)$ is modified (Eq. (13)), so that the two maxima of diffusivity can be represented with the modified scheme.

The NIWs and associated ocean mixing are greatly enhanced by strong winds, such as tropical cyclones and typhoon. The differences between the J13 scheme and the observations are pronounced during typhoon. Although the typhoon period is relatively short in a whole year, it has been well recognized that typhoon can play an important role in modulating the large-scale ocean heat content and circulation, as well as rectifying the global climate change (D'Asaro et al., 2014; Fedorov et al., 2010; Knutson et al., 2010; Zhang et al., 2020). Therefore, a better parameterization for NIWs is highly desired for ocean and climate models, and the modifications to the J13 scheme are proposed. Although they are not included in a model for testing yet, they have better matches with observations compared to the J13 scheme during typhoon. For example, the new parameterization for diffusivity can capture two peaks in the vertical and reproduce the time lag in NIWs above and below the boundary layer depth.

Besides the local impacts, remote forcing and meridional propagation of NIWs may also be important for the stratification before typhoon arrives, which has not been considered so far. Much more observations are also required for improving and calibrating the NIW parameterization, especially during strong winds like typhoon. The vertical resolution for traditional observations on ocean currents, temperature, and salinity should be increased in the upper several hundred meters, so that the boundary layer depth and the vertical shear can be well resolved. In addition, fine-structure measurements should be conducted during typhoon, so that the parameterized diapycnal mixing can be fully calibrated. Obviously, since typhoons are not conducive for *in-situ* observations, some novel autonomous technology and instruments will be greatly helpful. Besides observations, a better understanding of the dynamics of NIWs is also required. For example, the fast downward spreading of near-inertial energy below the upper boundary layer is well-documented in observations in the SCS, as well as in many previous studies (such as Jaimes and Shay, 2010; Levine and Zervakis, 1995; Simmons and Alford, 2012). However, the simulation and proper parameterization of such fast-downward spreading are still challenging, as indicated with current comparisons between the J13 scheme and the observations. Overall, a better understanding of the dynamics and dedicated observations of NIWs are necessary for designing a better parameterization of NIWs, which will benefit more accurate climate models in the future.

References

Alford M H. 2020. Revisiting near-inertial wind work: slab models, relative stress, and mixed layer deepening. Journal of Physical Oceanography, 50(11): 3141–3156, doi: 10.1175/JPO-D-20-0105.1

Alford M H, Cronin M F, Klymak J M. 2012. Annual cycle and depth penetration of wind-generated near-inertial internal waves at ocean station papa in the Northeast Pacific. Journal of Physical Oceanography, 42(6): 889–909, doi: 10.1175/JPO-D-11-092.1

Alford M H, Gregg M C. 2001. Near-inertial mixing: Modulation of shear, strain and microstructure at low latitude. Journal of Geophysical Research: Oceans, 106(C8): 16947–16968, doi: 10.1029/2000JC000370

Alford M H, MacKinnon J A, Simmons H L, et al. 2016. Near-inertial internal gravity waves in the ocean. Annual Review of Marine Science, 8: 95–123, doi: 10.1146/annurev-marine-010814-015746

Alford M H, Whitmont M. 2007. Seasonal and spatial variability of near-inertial kinetic energy from historical moored velocity records. Journal of Physical Oceanography, 37(8): 2022–2037, doi: 10.1175/JPO3106.1

Chen Gengxin, Xue Huijie, Wang Dongxiao, et al. 2013. Observed near-inertial kinetic energy in the northwestern South China Sea. Journal of Geophysical Research: Oceans, 118(10): 4965–4977, doi: 10.1002/jgrc.20371

D'Asaro E A. 1985. The energy flux from the wind to near-inertial motions in the surface mixed layer. Journal of Physical Oceanography, 15(8): 1043–1059, doi: 10.1175/1520-0485(1985)015<1043:TEFFTW>2.0.CO;2

D'Asaro E A. 1995. A collection of papers on the ocean storms experiment. Journal of Physical Oceanography, 25(11): 2817–2818, doi: 10.1175/1520-0485(1995)025<2817:ACOPOT>2.0.CO;2

D'Asaro E A, Black P G, Centurioni L R, et al. 2014. Impact of typhoons on the ocean in the Pacific. Bulletin of the American Meteorological Society, 95(9): 1405–1418, doi: 10.1175/BAMS-D-12-00104.1

D'Asaro E A, Eriksen C C, Levine M D, et al. 1995. Upper-ocean inertial currents forced by a strong storm. Part I: Data and comparisons with linear theory. Journal of Physical Oceanography, 25(11): 2909–2936, doi: 10.1175/1520-0485(1995)025<2909:UOICFB>2.0.CO;2

Fedorov A V, Brierley C M, Emanuel K. 2010. Tropical cyclones and permanent El Niño in the early Pliocene epoch. Nature, 463(7284): 1066–1070, doi: 10.1038/nature08831

Fleagle R G, Businger J A. 1980. An Introduction to Atmospheric Physics. New York, NY, USA: Academic Press

Fu L L. 1981. Observations and models of inertial waves in the deep ocean. Reviews of Geophysics, 19(1): 141–170, doi: 10.1029/RG019i001p00141

Furuichi N, Hibiya T, Niwa Y. 2008. Model-predicted distribution of wind-induced internal wave energy in the world's oceans. Journal of Geophysical Research: Oceans, 113: C09034

Hebert D, Moum J N. 1994. Decay of a near-inertial wave. Journal of Physical Oceanography, 24(11): 2334–2351, doi: 10.1175/1520-0485(1994)024<2334:DOANIW>2.0.CO;2

Jaimes B, Shay L K. 2010. Near-inertial wave wake of Hurricanes Katrina and Rita over mesoscale oceanic eddies. Journal of Physic-

al Oceanography, 40(6): 1320–1337, doi: 10.1175/2010JPO4309.1
Jochum M, Briegleb B P, Danabasoglu G, et al. 2013. The impact of oceanic near-inertial waves on climate. Journal of Climate, 26(9): 2833–2844, doi: 10.1175/JCLI-D-12-00181.1
Knutson T R, McBride J L, Chan J, et al. 2010. Tropical cyclones and climate change. Nature Geoscience, 3(3): 157–163, doi: 10.1038/ngeo779
Kunze E, Briscoe M G, Williams A J III. 1990. Interpreting shear and strain fine structure from a neutrally buoyant float. Journal of Geophysical Research: Oceans, 95(C10): 18111–18125, doi: 10.1029/JC095iC10p18111
Kunze E, Sanford T B. 1984. Observations of near-inertial waves in a front. Journal of Physical Oceanography, 14(3): 566–581, doi: 10.1175/1520-0485(1984)014<0566:OONIWI>2.0.CO;2
Large W G, Grawford G B. 1995. Observations and simulations of upper-ocean response to wind events during the Ocean Storms Experiment. Journal of Physical Oceanography, 25(11): 2831–2852, doi: 10.1175/1520-0485(1995)025<2831:OASOUO>2.0.CO;2
Large W G, McWilliams J C, Doney S C. 1994. Oceanic vertical mixing: A review and a model with a nonlocal boundary layer parameterization. Reviews of Geophysics, 32(4): 363–403, doi: 10.1029/94RG01872
Levine M D, Zervakis V. 1995. Near-inertial wave propagation into the pycnocline during ocean storms: observations and model comparison. Journal of Physical Oceanography, 25(11): 2890–2908, doi: 10.1175/1520-0485(1995)025<2890:NIWPIT>2.0.CO;2
Li Xinming, Qian Qingying. 1989. The wind stress field over the South China Sea. Journal of Ocean University of Qingdao, 19(3): 10–18
MacKinnon J A, Zhao Zhongxiang, Whalen C B, et al. 2017. Climate process team on internal wave-driven ocean mixing. Bulletin of the American Meteorological Society, 98(11): 2429–2454, doi: 10.1175/BAMS-D-16-0030.1
Munk W, Wunsch C. 1998. Abyssal recipes II: energetics of tidal and wind mixing. Deep-Sea Research Part I: Oceanographic Research Papers, 45(12): 1977–2010, doi: 10.1016/S0967-0637(98)00070-3
Olbers D, Eden C. 2013. A global model for the diapycnal diffusivity induced by internal gravity waves. Journal of Physical Oceanography, 43(8): 1759–1779, doi: 10.1175/JPO-D-12-0207.1
Osborn T R. 1980. Estimates of the local rate of vertical diffusion from dissipation measurements. Journal of Physical Oceanography, 10(1): 83–89, doi: 10.1175/1520-0485(1980)010<0083:EOTLRO>2.0.CO;2
Park J J, Kim K, Schmitt R W. 2009. Global distribution of the decay timescale of mixed layer inertial motions observed by satellite-tracked drifters. Journal of Geophysical Research, 114(C11): C11010, doi: 10.1029/2008JC005216
Pedlowsky J, Miles J W. 2004. Waves in the ocean and atmosphere: Introduction to wave dynamics. Applied Mechanics Reviews, 57(4): B20
Price J F. 1981. Upper ocean response to a hurricane. Journal of Physical Oceanography, 11(2): 153–175, doi: 10.1175/1520-0485(1981)011<0153:UORTAH>2.0.CO;2
Qi Hongbo, De Szoeke R A, Paulson C A, et al. 1995. The structure of near-inertial waves during ocean storms. Journal of Physical Oceanography, 25(11): 2853–2871, doi: 10.1175/1520-0485(1995)025<2853:TSONIW>2.0.CO;2
Sanford T B, Price J F, Girton J B. 2011. Upper-ocean response to Hurricane Frances (2004) observed by profiling EM-APEX floats. Journal of Physical Oceanography, 41(6): 1041–1056, doi: 10.1175/2010JPO4313.1
Silverthorne K E, Toole J M. 2009. Seasonal kinetic energy variability of near-inertial motions. Journal of Physical Oceanography, 39(4): 1035–1049, doi: 10.1175/2008JPO3920.1
Simmons H L, Alford M H. 2012. Simulating the long-range swell of internal waves generated by ocean storms. Oceanography, 25(2): 30–41, doi: 10.5670/oceanog.2012.39
Sloyan B M, Rintoul S R. 2001. The southern ocean limb of the global deep overturning circulation. Journal of Physical Oceanography, 31(1): 143–173, doi: 10.1175/1520-0485(2001)031<0143:TSOLOT>2.0.CO;2
Ten Doeschate A, Sutherland G, Esters L, et al. 2017. ASIP: profiling the upper ocean. Oceanography, 30(2): 33–35, doi: 10.5670/oceanog.2017.216
Troen I, Petersen E L. 1989. European Wind Atlas. Roskilde, Denmark: Risø National Laboratory
van Haren H, Gostiaux L. 2012. Energy release through internal wave breaking. Oceanography, 25(2): 124–131, doi: 10.5670/oceanog.2012.47
Wang Wei, Huang Rui Xin. 2004. Wind energy input to the Ekman layer. Journal of Physical Oceanography, 34(5): 1267–1275, doi: 10.1175/1520-0485(2004)034<1267:WEITTE>2.0.CO;2
Watanabe M, Hibiya T. 2002. Global estimates of the wind-induced energy flux to inertial motions in the surface mixed layer. Geophysical Research Letters, 29(8): 64-1–64-3
Webster F. 1968. Observations of inertial-period motions in the deep sea. Reviews of Geophysics, 6(4): 473–490, doi: 10.1029/RG006i004p00473
Wolk F, Yamazaki H, Seuront L, et al. 2002. A new free-fall profiler for measuring biophysical microstructure. Journal of Atmospheric and Oceanic Technology, 19(5): 780–793, doi: 10.1175/1520-0426(2002)019<0780:ANFFPF>2.0.CO;2
Wunsch C, Ferrari R. 2004. Vertical mixing, energy, and the general circulation of the oceans. Annual Review of Fluid Mechanics, 36: 281–314, doi: 10.1146/annurev.fluid.36.050802.122121
Ying Ming, Zhang Wei, Yu Hui, et al. 2014. An overview of the China meteorological administration tropical cyclone database. Journal of Atmospheric and Oceanic Technology, 31(2): 287–301, doi: 10.1175/JTECH-D-12-00119.1
Zhai Xiaoming, Greatbatch R J, Eden C. 2007. Spreading of near-inertial energy in a 1/12° model of the North Atlantic Ocean. Geophysical Research Letters, 34(10): L10609, doi: 10.1029/2007GL029895
Zhang Han, Chen Dake, Zhou Lei, et al. 2016. Upper ocean response to typhoon Kalmaegi (2014). Journal of Geophysical Research: Oceans, 121(8): 6520–6535, doi: 10.1002/2016JC012064
Zhang Han, Wu Renhao, Chen Dake, et al. 2018. Net modulation of upper ocean thermal structure by Typhoon Kalmaegi (2014). Journal of Geophysical Research: Oceans, 123(10): 7154–7171, doi: 10.1029/2018JC014119
Zhang Yu, Zhang Zhengguang, Chen Dake, et al. 2020. Strengthening of the Kuroshio current by intensifying tropical cyclones. Science, 368(6494): 988–993, doi: 10.1126/science.aax5758